

Non-Ionic Deep Learning-Driven IR-UWB Multiantenna Scheme for Breast Tumor Localization

PATTARAPONG PHASUKKIT^{ID}, (Member, IEEE)

School of Engineering, King Mongkut's Institute of Technology Ladkrabang, Bangkok 10520, Thailand

e-mail: pattarapong.ph@kmitl.ac.th

This work was supported in part by the King Mongkut's Institute of Technology Ladkrabang (KMITL) Research and Innovation Services (KRIS) of King Mongkut's Institute of Technology Ladkrabang.

ABSTRACT This research proposes a deep learning-driven impulse radio ultra-wideband (IR-UWB) multiantenna scheme for non-ionic breast tumor localization. The structure of the multiantenna scheme consists of one side slot Vivaldi transmitting (Tx) and nine side slot Vivaldi receiving (Rx₁ – Rx₉) antennas. To mitigate the attenuation and improve the diagnostic accuracy, the multiantenna scheme is rotated clockwise in 90° increments around the breast, with the angular position of the Tx antenna of 0°, 90°, 180°, and 270°. The deep learning algorithm is utilized to detect and localize the breast tumor, with 17 classification outputs, consisting of classifications 1 – 16 which correspond to 16 vertically discretized segments of the breast and classification 17 for cancer-free. Experiments were carried out using heterogenous breast replicas with a tumor of 1 cm in diameter, and the breast replicas possess the dielectric property and Hounsfield units (HU) similar to those of human breasts. The experimental results were compared with the computed tomography (CT) scan images. The results reveal that the multiantenna scheme could efficiently detect and accurately localize the breast tumor for nearly all classifications, with the total accuracy (average of F1 scores) of 99.11 %. Specifically, the novelty of this research lies in the use of deep learning with the IR-UWB technology to effectively localize breast tumors.

INDEX TERMS Deep learning, breast tumor localization, IR-UWB, multiantenna, breast replica.

I. INTRODUCTION

Globally breast cancer is one of the leading causes of untimely death for women, claiming more than 1.8 million lives annually [1]. As a result, early detection of breast cancer or tumors is critical to effective treatment, given a 97 % survival rate [2].

Existing ionic cancer diagnostic technologies, including X-ray mammography, computed tomography (CT), and magnetic resonance imaging (MRI), normally yield low-resolution images and require human interpretation, rendering it susceptible to interpretation error. Besides, the ionic cancer diagnostic technologies subject the patients to ionizing radiation. Specifically, when ionizing radiation interacts with cells, it can cause damage to the cells and genetic material (i.e., deoxyribonucleic acid or DNA). Such damage can result in cell death or harmful changes in the DNA. The detectability

of the existing diagnostic technologies is also impeded for tumors residing deep inside the breast. Furthermore, the diagnostic time of the ionic technologies is relatively lengthy.

In [3] and [4], a combination of X-ray mammography and MRI was employed to diagnose patients with benign and malignant tumors. The combined scheme however achieved an accuracy rate of merely 75.6 %, revealing certain flaws inherent in the current technologies (i.e., expertise and experience of the radiologists). Meanwhile, to address the issue of ionization associated with the ionic cancer diagnostic technologies, non-ionizing diagnostic techniques based on microwave imaging (MWI, 0.3 – 300 GHz) and terahertz (THz, 0.3 – 10 THz) radiography have been developed and proposed as an alternative to the existing diagnostic techniques [5]. The MWI and THz technologies produce high-resolution images but the technologies are complex and cumbersome [6].

The associate editor coordinating the review of this manuscript and approving it for publication was Sung-Min Park^{ID}.

Unlike the ionic diagnostic systems, the non-ionizing THz radiography causes minimal harm to human health, particularly in the lower frequency band; and is sensitive to water-absorption tissue cells. However, the THz radiography encounters several drawbacks, including high attenuation due to low transmitting power of less than one μW per dose and black body radiation at room temperature. Besides, the ionization risks increase with increase in THz frequency. In comparison, the THz radiography is more complicated and costlier than MWI [7].

In [8], ultra-wideband (UWB) microwave imaging with Bayesian inverse scattering algorithm was proposed for detection of breast tumors. In [9], simulations were carried out using electromagnetic (EM) waves with a feed-forward backpropagation neural network model to detect and localize early-stage breast cancer/tumors.

In [10], support vector machine (SVM)-based UWB technology was used to classify breast tumors into two categories: cancerous and cancer-free. In [11], the authors investigated the cancer growth over time using SVM based on UWB backscattered signals from successive scans of a dielectrically heterogeneous breast.

In [12], radar-based UWB microwave imaging was first applied to clinically diagnose breast tumors in patients. In [13], radar-based UWB technology was used to detect tumors of varying sizes in breast replicas, with the smallest tumor of 1 cm in diameter. In [14], the convolution neural network (CNN) was used to diagnose medical images of breasts for tumors. In [15] and [16], the UWB technology together with K-nearest neighbors was used to detect the presence of breast cancer, but the technology is unable to localize the cancerous cells.

In [17], UWB microwave imaging was used to visualize the locations of cancer in breast replicas. In [18], an SVM-based flexible antenna scheme that fits the breast configuration was proposed to detect breast tumors. In [19], the UWB radar system with SVM was proposed to detect breast tumors of varying shapes and sizes.

Specifically, the ionizing radiation technologies, e.g., X-ray mammography, MRI, and CT scan, yield low-resolution images and chiefly rely on human interpretation for diagnostic results. Besides, the ionic technologies subject the patients to ionization risks and potential health hazards. Meanwhile, the capability of the existing non-ionizing UWB technologies for breast tumor detection, e.g., SVM, K-nearest neighbors-based schemes, are severely limited.

The rationale behind using impulse radio ultra-wideband (IR-UWB) signal for breast tumor localization is that the IR-UWB technology is low-cost and non-ionic, with high-resolution image quality. IR-UWB propagates short-pulse microwave signal with high penetration, rendering it operationally applicable to detecting small tumors in the breast. In addition, the IR-UWB technique identifies the breast tumor by the differential between the dielectric constants of the malignant and normal tissues (by the ratio of 5:1); and by the differential between the conductivity

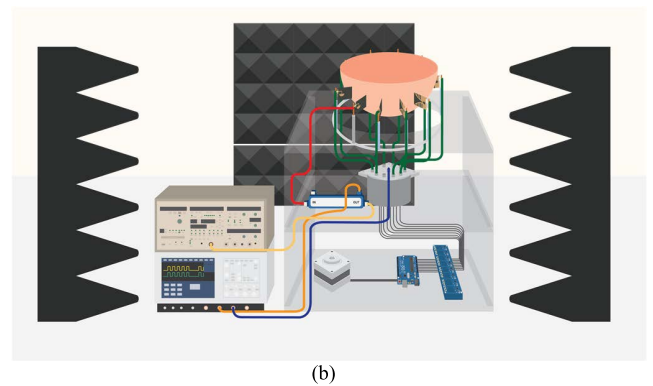
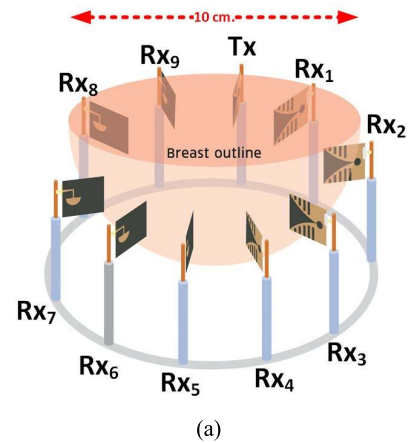


FIGURE 1. The proposed IR-UWB multiantenna scheme: (a) Tx and Rx₁ – Rx₉ antennas with breast outline, (b) the schematic of the proposed multiantenna scheme with the main components.

of the malignant and normal tissues (by the ratio of 10:1) [20]–[23].

As a result, this research proposes a non-ionic deep learning-driven IR-UWB multiantenna scheme to detect and localize breast tumors. The proposed multiantenna scheme consists of one transmitting and nine receiving antennas. Unlike the existing breast tumor detection schemes, deep learning algorithm is incorporated into the proposed multiantenna scheme to efficiently detect and accurately localize the breast tumor. In addition, experiments were carried out using heterogeneous breast replicas and results compared with the CT scan images.

II. IR-UWB MULTIAN TENNA SCHEME FOR BREAST TUMOR LOCALIZATION

The structure of the proposed IR-UWB multiantenna scheme for breast tumor localization is of 10 side slot Vivaldi antennas, consisting of one transmitting (Tx) antenna and nine receiving (Rx) antennas (Rx₁ – Rx₉), as shown in Fig. 1(a). The antennas (Tx and Rx₁ – Rx₉) are uniformly and angularly arranged (individually at 36°) to encircle the patient's breast during diagnosis. In this research, the Tx and Rx antennas are of side slot Vivaldi type, following [29], with the impedance bandwidth between 2.8–7.0 GHz and the antenna gain of 6 dBi (Table 3). The antenna substrate is of

Rogers RT/duroid 5870, with 35 μm copper on either side and 1.57 mm in height. The relative permittivity and loss tangent of the substrate are 2.33 and 0.0012.

The inner diameter of the multiantenna scheme is adjustable to fit the patient's breast, with the largest inner diameter of 10 cm. In the experiment, the tumor size is 1 cm in diameter [14].

In Fig. 1(b), the Tx antenna is connected to an IR-UWB source (Anritsu MP1763C), and the Rx₁ – Rx₉ antennas are connected to an RF-Switch (DOW-Key Microwave 5A1-5208). The signals from Rx₁ – Rx₉ antennas are subsequently fed to a digital oscilloscope (Tektronix TDS7404B) whose function is to convert analog to digital signal (ADC). The walls of the multiantenna scheme are lined with the anechoic absorbers.

In the breast tumor diagnosis, the 10 antennas (Tx and Rx₁ – Rx₉) of the proposed multiantenna scheme are rotated clockwise by a stepping motor in 90° increments around the breast, consisting of four rotating steps with the angular position of the Tx antenna at 0° for the first rotating step, at 90° for the second rotating step, at 180° for the third rotating step, and at 270° for the last rotating step. Since attenuation increases with the distance between the Tx antenna and tumor, the circular rotation of the Tx antenna is utilized to mitigate the attenuation of transmitting signals while improving the tumor detection accuracy.

Given the nine Rx antennas (Rx₁, Rx₂, Rx₃, . . . , Rx₉) and four angular positions of Tx antenna (0°, 90°, 180°, 270°), the number of received signals of the multiantenna scheme is 36 per round of scanning of one single breast (i.e., 36 received signals per round per breast). In addition, deep learning algorithms are utilized to efficiently localize breast tumors.

Fig. 2 shows the IR-UWB signal in time and frequency domain. In this research, the IR-UWB signal is generated by a pulse/pattern generator (Anritsu MP1763C) with a pulse width 0.56 ns. The pulse repetition frequency (PRF) as measured by the digital oscilloscope (Tektronix TDS7404B) is 20 MHz, and the amplitude of the operating frequency is verified by a spectrum analyzer (Anritsu MS8609A). The IR-UWB bandwidth is between 110MHz – 3.125 GHz, given the Federal Communications Commission's (FCC) normalized magnitude of ≥ -10 dB. The fractional bandwidth is 1.864, given the FCC's UWB criterion of ≥ 0.25 . As a result, the transmitting signal emitted from the Tx antenna is of UWB.

Fig. 3 graphically illustrates the diagnosis of breast tumor using the non-ionic IR-UWB multiantenna scheme where the patient lies on top of the proposed multiantenna scheme in the prone position. The multiantenna scheme for breast tumor localization is outfitted from the underneath through the opening in the examination bed. In the breast tumor diagnosis, the non-ionic multiantenna scheme is hydraulically lifted from underneath the examination bed and fitted to either breast. Once the examination is complete, the antenna scheme is hydraulically retracted and motioned to fit the other breast. The examination time is between 1 – 2 minutes per breast.

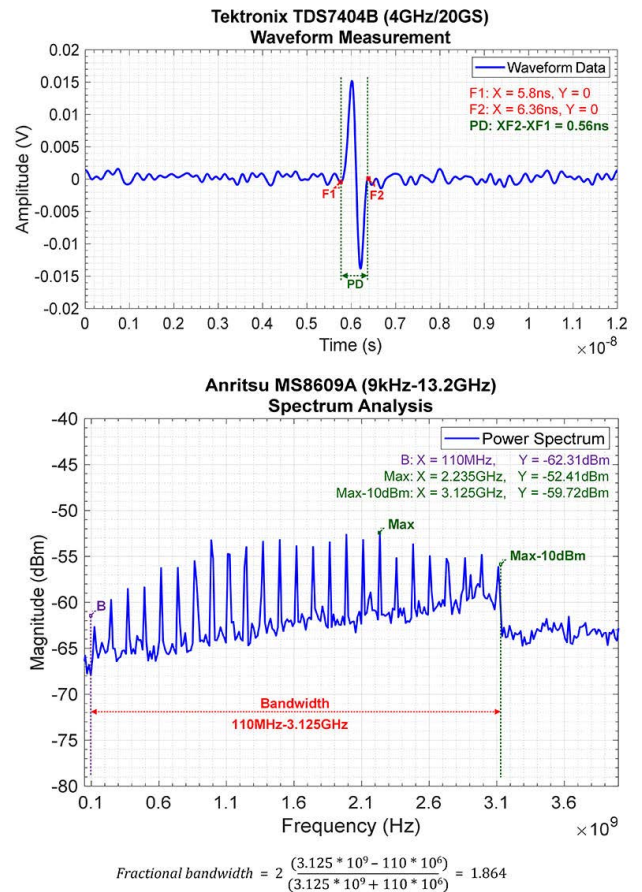


FIGURE 2. Impulse radio ultra-wideband (IR-UWB) signal in time domain and frequency.



FIGURE 3. The diagnosis of breast tumor using the non-ionic deep learning-driven IR-UWB multiantenna scheme.

Fig. 4 illustrates the operation principle of the deep learning-driven IR-UWB multiantenna scheme for breast tumor localization. The multiantenna scheme consists of one Tx and nine Rx₁ – Rx₉ antennas encircling the diagnostic breast. This research used the breast replicas of semicircular shape with almost identical dielectric properties [24] and

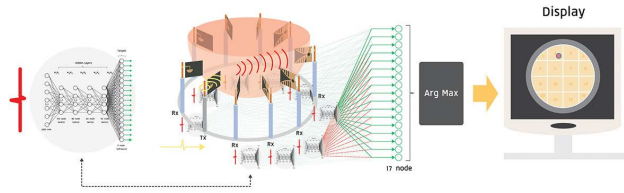


FIGURE 4. The operation principle of the deep learning-driven IR-UWB multiantenna scheme for breast tumor localization.

Hounsfield units (HU) [25]–[27] to those of the real women’s breasts. The HU is a relative quantitative measurement of radio density used by radiologists in the interpretation of CT images.

As shown in Fig. 3, given the Tx angular position of 0°, the Tx antenna first transmits IR-UWB signal (2.0 – 7.0 GHz) through the breast replica to the nine Rx antennas (Rx₁ – Rx₉). The received signals are then independently processed by the deep learning algorithms of nine different receiving antennas. Specifically, the received signals (i.e., input data) of Rx₁, Rx₂, . . . , Rx₉ are independently processed by the deep learning algorithm of Rx₁, Rx₂, . . . , and Rx₉, respectively. Each Rx antenna (Rx₁ – Rx₉) yields 17 classification outputs (i.e., 17 classifications), consisting of classifications 1 – 16 which correspond to locations 1 – 16 of the tumors in the breast replicas and classification 17 for cancer-free. The aforementioned procedure is repeated at Tx = 90°, 180°, and 270°. In this research, the breast is vertically discretized (along the breast length) into 16 segments and labeled classifications 1 – 16. The segmentation of the breast is to be discussed in subsequent section.

In the operation, the received signal by each receiving antenna (Rx₁, Rx₂, Rx₃, . . . , Rx₉) at Tx = 0°, 90°, 180°, and 270° is individually converted by the digital oscilloscope (Tektronix 7404B) into 50,000 data points. For example, the received signals by the Rx₁ antenna at Tx = 0°, 90°, 180°, and 270° are individually converted into 50,000 data points, i.e., 50,000 data points each for Tx = 0°, 90°, 180°, and 270°. The data points of each receiving antenna (50,000 data points) at different Tx angular positions (0°, 90°, 180°, and 270°) are the data input (i.e., feature) of the deep learning algorithm of the respective receiving antenna, and there are 50,000 input nodes for each receiving antenna. The number of deep learning output nodes for each receiving antenna (Rx₁, Rx₂, Rx₃, . . . , Rx₉) at each Tx angular position (0°, 90°, 180°, and 270°) is 17 (i.e., 17 classifications), corresponding to locations 1 – 16 of the tumor in the breast replicas and classification 17 for cancer-free. The deep learning outputs are in the probabilistic form, indicating the probability of the presence or absence of tumor in different locations of the breast.

III. BREAST REPLICAS AND DIELECTRIC PROPERTIES

In this research, the fabrication of heterogenous breast replicas followed [28], [29], consisting of four layers: skin,

TABLE 1. Composition of the heterogeneous breast replica [24].

Material	Quantity			
	Skin	Fat	Gland	Tumor
Distilled water	80 ml	40 ml	80ml	100 ml
Safflower oil	14 ml	39 ml	21 ml	7 ml
Propylene glycol	7 ml	2 ml	7 ml	6.5 ml
Agar agar-gelatin powder	5.88 g	7 g	5 g	9 g
Formalin (37 % formaldehyde solution)	0.3 ml	0.3 ml	0.3 ml	0.3 ml
Xanthan gum	1.3 g	1.3 g	1.3 g	1.3 g
Liquid detergent	0.3 ml	0.3 ml	0.3 ml	0.3 ml

fat, gland, and tumor. Table 1 tabulates the composition of the four layers of the heterogenous breast replicas. In the development of breast replicas, the materials (Table 1) were mixed thoroughly in a vat thermally treated at approximately 60°C for 5 min. The mixtures were sequentially transferred to a mold (starting with the skin layer, fat layer, gland and tumor) and left to cool down to room temperature (25°C). A vector network analyzer (VNA, HP 8720B) was used to measure the reflection coefficients (S₁₁) of different tissue layers of the breast replica, and the dielectric properties of different tissue layers were determined following [29].

In the measurement of S₁₁ of different tissue layers of the breast replica, the VNA with an open-ended coaxial probe, given the UWB frequency of 2.0 – 7.0 GHz, was used to determine the reflection coefficients (S₁₁). Prior to the measurement, the open-ended coaxial probe was first calibrated by using the calibration kit. The S₁₁ of distilled water was subsequently measured using the calibrated VNA, given the known dielectric (ε_c) of 80 [30]; and the complex admittance (Y_{admittance}) of distilled water was determined by using (1) [31]. Substituting Y_{admittance} and ε_c in (2) yields the constant values C₀ and G₀, which were subsequently used to calculate the dielectrics of different tissue layers of the cancer-free breast replica.

The dielectrics of different tissue layers of the breast replica (i.e., skin, fat, gland, tumor) were independently determined. Specifically, the dielectric of the skin of the breast replica was first determined, separately followed by those of fat, gland, and finally tumor (Table 1).

In determining the dielectrics of different tissue layers, the S₁₁ of different tissue layers (skin, fat, gland, tumor) were first measured using the VNA, given 2.0 – 7.0 GHz; and their respective complex admittance (Y) were determined by using (1), where Y_{probe} is the admittance of the probe which is equal to 0.02 (i.e., 1/50 Ω)

$$Y = Y_0 \frac{1 - S_{11}}{1 + S_{11}} \tag{1}$$

TABLE 2. Dielectric and hounsfield unit of different tissue layers of the real breast and breast replica.

Tissue layer	Dielectric Properties					
	Permittivity (F/m)		Conductivity (S/m)		Hounsfield unit (HU)*	
	Real breast [24]	Breast replica	Real breast [24]	Breast replica	Real breast [25,26,27]	Breast replica
Skin	36	35.21	4	4.2	5	7
Fat	9	10.31	0.4	0.5	6	8
Gland	11-15	12.04	0.4-0.5	0.48	11	13
Tumor	50	51.05	4	4.2	60	61

Note: * HU was measured by a CT machine (Siemens, SOMATOM Confidence).

To calculate the dielectrics (ϵ_c) of different tissue layers of the breast replica, substitute $Y_{\text{admittance}}$, C_0 and G_0 in (2), where $\epsilon_c = \epsilon'_r - j\epsilon''_r$ where ϵ'_r is the real part of dielectric (i.e., permittivity) and $j\epsilon''_r$ is the imaginary part of dielectric (i.e., conductivity or the loss factor) [32].

$$Y = j\omega\epsilon_c C_0 + \sqrt{\epsilon_c} G_0 \tag{2}$$

where [33].

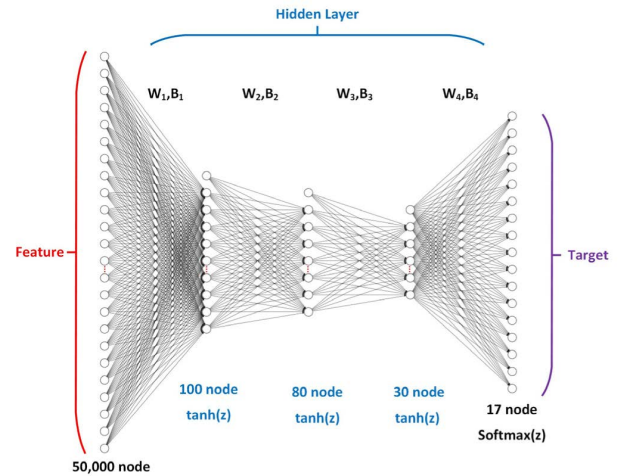
$$C_0 = \left(1.04709527791738 \times 10^{-15} \right) - j(9.14281380831597 \times 10^{-15}),$$

$$G_0 = \left(1.94797446126132 \times 10^{-7} \right) - j(5.70866416183116 \times 10^{-8}),$$

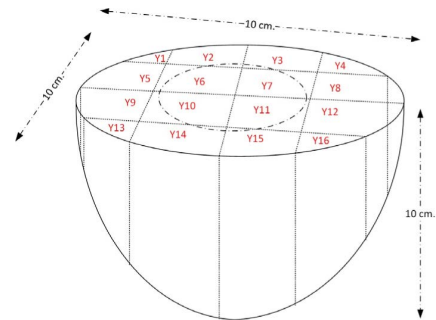
and $\omega = 2\pi f$ where f is the frequency range between 2.0 – 7.0 GHz.

For ease of calculation of ϵ_c in (2), go to www.wolframalpha.com to access the Mathematica software for online solving of the complex equation free-of-charge. The software always returns three values of ϵ_c , consisting of one positive and two negatives. Since the dielectric must be a positive value, the positive ϵ_c is selected for different tissue layers of the breast replica.

Table 2 tabulates the dielectric properties and Hounsfield unit (HU) of different tissue layers of the real breast and breast replica. The HU is a relative quantitative measurement of radio density used by radiologists in the interpretation of CT images. As shown in the table, the dielectric properties (permittivity and conductivity) and HU of the breast replica closely resemble those of the real breast, indicating that the breast replica could be used as substitute for the real breast in the breast tumor localization experiments.



(a)



(b)

FIGURE 5. The deep learning algorithm for breast tumor localization: (a) the algorithmic scheme, (b) the vertically discretized breast into 16 segments.

IV. DEEP LEARNING ALGORITHM FOR BREAST TUMOR LOCALIZATION

A. DEEP LEARNING ALGORITHM AND DISCRETIZED BREAST

In this research, the deep learning algorithm consists of three principal layers: the input layer (feature), hidden layer (four hidden layers in total), and output layer (target), as shown in Fig. 5 (a). In the input layer, there are 50,000 nodes for each received signal from each Rx antenna (Rx_1, Rx_2, \dots, Rx_9) at each Tx angular position ($0^\circ, 90^\circ, 180^\circ, 270^\circ$).

The input (50,000 data points) are fed into the first hidden layer, given the weight and bias of W_1 and B_1 ; and there are 100 nodes in the first hidden layer. The output of the first hidden layer are then fed into 80 nodes of the second hidden layer, given W_2 and B_2 . The output of the second hidden layer are fed into 60 nodes of the third hidden layer, given W_3 and B_3 ; and subsequently to the fourth hidden layer with 30 nodes, given W_4 and B_4 . The weight and bias (W and B) for each Rx antenna (Rx_1, Rx_2, \dots, Rx_9) at each Tx angular position ($0^\circ, 90^\circ, 180^\circ, 270^\circ$) are independently optimized by gradient descent iterative optimization algorithm. The hyperbolic tangent (*Tanh*) is the activation function in the four hidden layers, with the values between $[-1, 1]$.

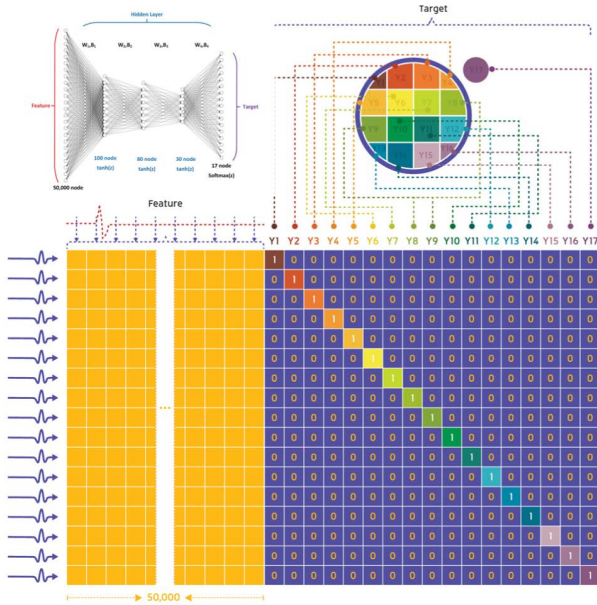


FIGURE 6. The data structure of the proposed deep learning algorithm at any given Rx antenna (Rx₁, Rx₂, . . . , or Rx₉) and angular Tx position (i.e., 0°, 90°, 180°, or 270°).

In the output layer (target), there are 17 output nodes (Y1 – Y17) for each Rx antenna (Rx₁, Rx₂, . . . , Rx₉) at each Tx angular position (0°, 90°, 180°, 270°), with *SoftMax* as the activation function. The output nodes Y1 – Y17 correspond to classifications 1 – 17, where classifications 1 – 16 refer to locations 1 – 16 of the tumor in the breast and classification 17 to cancer-free. The deep learning outputs of the output nodes Y1 – Y17 are in probabilistic values. Specifically, the breast is vertically discretized (along the breast length) into 16 segments (Y1 – Y16) and labeled classifications 1 – 16, as shown in Fig. 5 (b).

Fig. 6 illustrates the data structure of the deep learning algorithm of any given Rx antenna (Rx₁, Rx₂, . . . , or Rx₉) and any given Tx angular position (0°, 90°, 180°, or 270°). In the Fig., the orange-hued cells, as an example, represent the total input data (feature) of Rx₁ antenna at Tx = 0°, and the rows in ascending order correspond to classifications 1 – 17. In other words, the first 16 rows correspond to the 16 discretized segments of the breast (Y1 – Y16) and the last row corresponds to classification 17, which is free of cancer. Each row of orange-hued cells, representing one received signal, consists of 50,000 data points. The data points are independently processed by the deep learning algorithms of the respective receiving antennas. In other words, the input data of Rx₁, Rx₂, . . . , and Rx₉ are independently processed by the deep learning algorithms of Rx₁, Rx₂, . . . , and Rx₉, respectively.

In the diagnosis, the multiantenna scheme is rotated clockwise by the stepping motor, with the Tx antenna angularly positioned at 0°, 90°, 180°, and 270°. As a result, the total number of datasets for one Rx antenna

(Rx₁, Rx₂, . . . , or Rx₉) at four Tx angular positions is 68, consisting of 17 datasets each for Tx at 0°, 90°, 180°, and 270°, where one dataset corresponds to one classification (i.e., classifications 1, 2, 3, . . . , 17).

Prior to training and testing the algorithms, the number of datasets for each Rx antenna at four Tx positions are deliberately mimicked 100 times using additive white gaussian noise (AWGN) to 6800 datasets. The additive datasets (6800 datasets) of each Rx antenna at four Tx positions are subsequently divided into two groupings: training (80 %) and testing (20 %). As a result, the training and testing groupings consist of 5440 and 1360 datasets, respectively. Given 17 classifications of the deep learning outputs (classifications 1 – 17), there are 3200 datasets per classification (5440 ÷ 17) for training and 80 datasets per classification (1360 ÷ 17) for testing the deep learning algorithm.

In the training, the weight (W) and bias (B) of the hidden layers of the deep learning algorithm (W₁, B₁, W₂, B₂, W₃, B₃, W₄, B₄) are optimized by gradient descent iterative optimization algorithm, given the learning rate (α) and epoch of 0.1 and 1000, respectively. Besides, in the training process, *L1-norm* regularization is used to avoid overfitting due to excessive data points (50,000 data points per Rx signal), and the iteration is terminated once the cross-entropy loss of the training- and testing-datasets diverge.

In addition, prior to the training and testing the deep learning algorithm, the training and testing datasets (both input and output datasets) are normalized using standardization in (3)

$$Standardization = \frac{Dataset - Mean\ of\ Dataset}{SD} \quad (3)$$

where *Dataset* is input and output datasets (i.e., X_{train} , Y_{train} , X_{test} , Y_{test}), *Mean of Dataset* is the mean value of input and output datasets, and SD is standard deviation.

In the feedforward, the hyperbolic tangent function ($tanh(z)$) is the activation function between hidden layers, as shown in (4) where $tanh(z) = [-1,1]$. The activation function *Softmax*(z) is used in the output layer, as shown in (5), where z is the linear combination (6). The deep learning output is in probabilistic values.

$$tanh(z) = \frac{(e^z - e^{-z})}{(e^z + e^{-z})} \quad (4)$$

$$\hat{Y}_n = Softmax(z) = \frac{e^{z_i}}{\sum_{j=1}^k e^{z_j}} \quad (5)$$

$$Z = \begin{bmatrix} z_1 \\ z_2 \\ \vdots \\ z_N \end{bmatrix} = \begin{bmatrix} x_1^1 w_1 & x_1^2 w_2 & \dots & x_1^D w_D \\ x_2^1 w_1 & x_2^2 w_2 & \dots & x_2^D w_D \\ \vdots & \vdots & \vdots & \vdots \\ x_N^1 w_1 & x_N^2 w_2 & \dots & x_N^D w_D \end{bmatrix} + [B_1 \ B_2 \ \dots \ B_D] \quad (6)$$

In the backpropagation, the cross-entropy between the normalized training output dataset (Y_{train} ; Y_n) and predicted normalized output (\hat{Y}_n) is first calculated using (7).

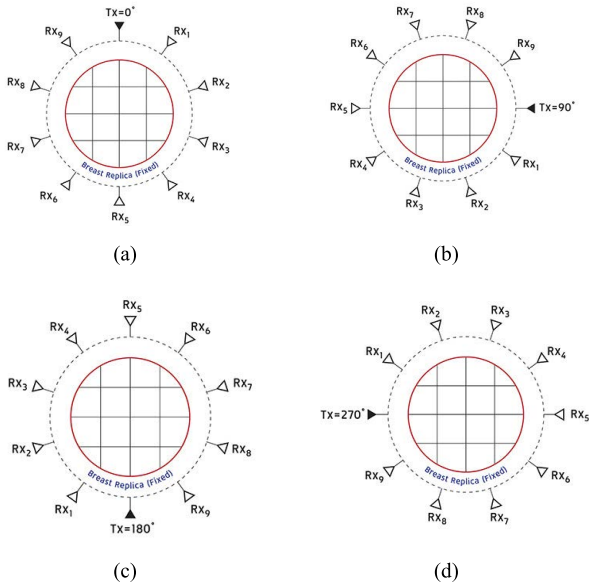


FIGURE 7. The schematic of the multiantenna scheme at four Tx angular positions: (a) Tx = 0°, (b) Tx = 90°, (c) Tx = 180°, (d) Tx = 270°.

The gradient descent iterative optimization algorithm is applied to optimize W and B by using (8) and the chain rule derivative.

$$J(w) = -\frac{1}{N} \sum_{n=1}^N (Y_n \log(\hat{Y}_n)) \quad (7)$$

where Y_n is true output value and \hat{Y}_n is predicted output value.

$$\frac{\partial J(w)}{\partial W_i} \text{ and } \frac{\partial J(w)}{\partial B_i} \quad (8)$$

where $i = 1, 2, 3, 4$ corresponding to $W_1, B_1, W_2, B_2, W_3, B_3, W_4, B_4$; and the derivative of the $\tanh(z)$ activation function for hidden layers is expressed in (9).

$$\frac{\partial[\tanh(z)]}{\partial z} = 1 - (\tanh(z))^2 \quad (9)$$

Fig. 7 (a) – (d) illustrate the schematics of the proposed deep learning-driven IR-UWB multiantenna scheme for breast tumor localization at four Tx angular positions (0°, 90°, 180°, 270°), respectively. In the diagnosis, the multiantenna scheme is rotated clockwise in 90° increments and the scanning is carried out, given the Tx angular positions of 0°, 90°, 180°, and 270°.

Fig. 8 illustrates the diagram of the deep learning algorithm of the proposed IR-UWB multiantenna scheme by classification (classifications 1, 2, . . . , or 17) for any given Rx antenna (Rx₁, Rx₂,. . . or Rx₉) at Tx of 0°, 90°, 180°, and 270°. Take the Rx₁ antenna as an example. Following Fig. 8, the received signals by Rx₁ antenna at Tx of 0°, 90°, 180°, and 270° are first normalized and then input into the deep learning algorithmic scheme to derive the summation of probabilistic values by classification at Tx of 0°, 90°, 180°, and 270° of Rx₁ antenna.

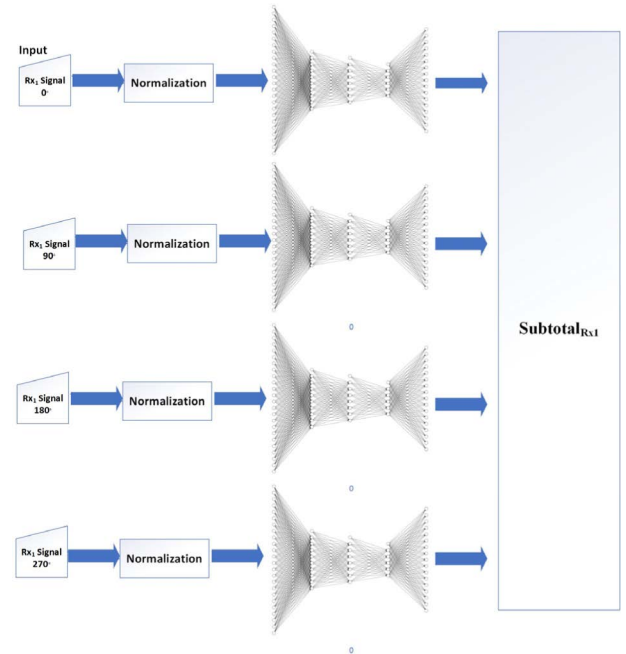


FIGURE 8. The diagram of the deep learning algorithm by classification (classifications 1, 2, . . . , or 17) for any given Rx antenna (Rx₁, Rx₂,. . . or Rx₉) at Tx of 0°, 90°, 180°, 270°.

Specifically, The probabilistic values of classification 1 of Rx₁ antenna at four Tx angular positions (0°, 90°, 180°, and 270°) are summed up to obtain the combined probabilistic values of classification 1 of Rx₁ antenna. The probabilistic values of classification 1 of Rx₁ antenna at Tx of 0°, 90°, 180°, and 270° are then retained in the computer memory. The same procedure is applied to derive the probabilistic values of the remaining classifications (classifications 2 – 17) at the four Tx angular positions of Rx₁ antenna. The probabilistic values of classifications 2 – 17 of Rx₁ antenna at four Tx angular positions are summed up to obtain the combined probabilistic values of classifications 2 – 17 of Rx₁ antenna. The aforementioned procedure yields the total probabilistic values for 17 classifications (classifications 1 - 17) of Rx₁ antenna, given Tx of 0°, 90°, 180°, and 270° (i.e., Subtotal_{Rx1}).

In the operation, apart from those of classifications 1 – 17 of Rx₁ antenna (as discussed above), the probabilistic values of classifications 1 – 17 of each of the remaining Rx antennas (Rx₂ – Rx₉) at four Tx angular positions (0°, 90°, 180°, 270°) are also independently summed up to obtain the combined probabilistic values of classifications 1 – 17 of Rx₂ – Rx₉ antennas. Likewise, the aforementioned procedure yields the total probabilistic values for 17 classifications of Rx₂ – Rx₉ antennas, given Tx of 0°, 90°, 180°, and 270° (i.e., Subtotal_{Rx2} – Subtotal_{Rx9}).

Furthermore, the combined probabilistic values by classification (classifications 1 – 17) of all nine receiving antennas (Rx₁ – Rx₉) are tallied to obtain the grand total probabilistic values by classification of the proposed multiantenna scheme (i.e., GrandTotal). There are 17 GrandTotal values by

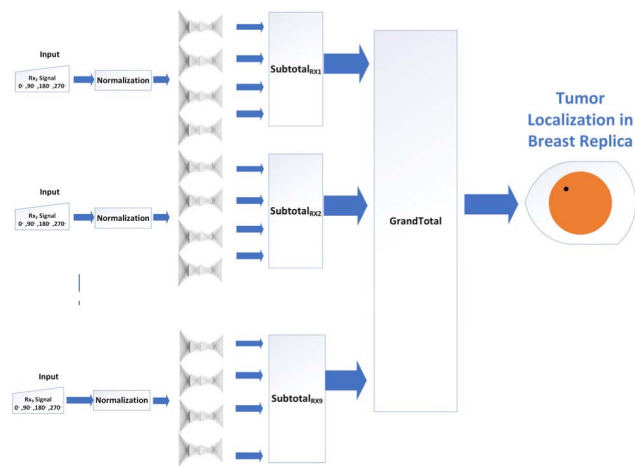


FIGURE 9. The overall schematic of the proposed deep learning algorithmic scheme for breast tumor localization.

classification, corresponding to the 16 discretized segments of the breast (classifications 1 – 16) and classification 17 for cancer-free. In the breast tumor localization, the deep learning algorithm selects the classification with the maximum probabilistic value (i.e., maximum GrandTotal). Fig. 9 shows the overall schematic of the proposed deep learning algorithm for breast tumor localization.

B. DEEP LEARNING ALGORITHM EVALUATION

The tumor localization performance of the proposed deep learning-driven IR-UWB multiantenna scheme is evaluated using the testing datasets. There are 8 datasets per classification for testing the algorithm, given 17 classifications (classifications 1 – 17) where classifications 1 – 16 correspond to the 16 discretized segments of the breast and classification 17 for cancer-free. (Note: See sub-section A above for details of the testing datasets.) In this research, the performance metrics include F1 score and total accuracy (average of F1 scores).

F1 score is a value that indicates the classification performance of an algorithmic model based on Precision (10) and Recall (11). The F1-score and total accuracy (average of F1 scores) can be calculated by (12) and (13), respectively.

$$Precision = \frac{TP}{TP + FP} \tag{10}$$

$$Recall = \frac{TP}{TP + FN} \tag{11}$$

where *TP* is the number of true positives, *FP* is the number of false positives, and *FN* is the number of false negatives.

In this research, true positive (*TP*) means that the deep learning algorithm is able to detect and correctly localizes the tumor for classifications 1 – 16 (corresponding to the 16 discretized segments of the breast). Meanwhile, for classification 17, *TP* means that the deep learning algorithm correctly identifies the breast as cancer-free. As previously stated, the breast tumor locations correspond to the 16 discretized segments of the breast (classifications 1 – 16).

False positive (*FP*), in case of classifications 1 – 16, means that either (a) the deep learning algorithm is able to detect the tumor but erroneously localizes it (for example, the actual location of the tumor is in segment 1 of the discretized breast, but the algorithm localizes the tumor to be in any other segment (i.e., segments 2 – 16) except segment 1); or (b) the algorithm fails to detect the tumor and consequently wrongly assigns the diagnostic breast to classification 17 (cancer-free). Meanwhile, in case of classification 17, *FP* means that the deep learning algorithm erroneously identifies the cancer-free breast as cancerous breast.

False negative (*FN*) means that, in case of classifications 1 – 16, the deep learning algorithm is able to detect the tumor but erroneously localizes it (for example, in *FN* (which is contrary to *FP*), the algorithm returns segment 1 as the tumor location although the actual location of the tumor is in other segments (segments 2 – 16). Meanwhile, in case of classification 17, *FN* means that the deep learning algorithm fails to detect the tumor and thus erroneously identifies the breast as cancer-free.

$$F1\ Score = 2x \frac{Precision * Recall}{Precision + Recall} \tag{12}$$

$$Total\ Accuracy\ (average\ F1\ Score) = \frac{(F1\ Score\ (class\ 1) + (F1\ Score\ (class\ 2) + (F1\ Score\ (class\ 3) + \dots (F1\ Score\ (class\ 17))}{17} \tag{13}$$

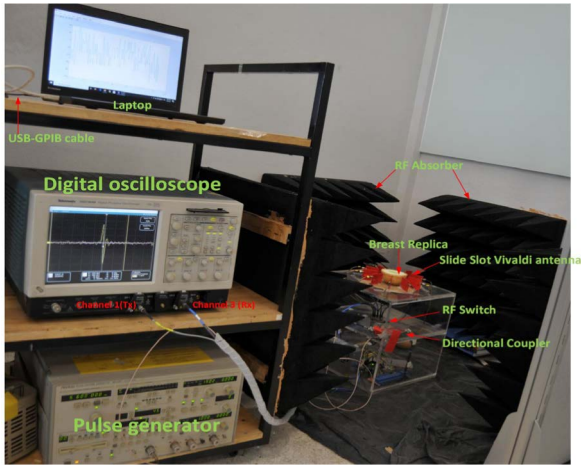
V. IN VITRO EXPERIMENTAL SETUP

Table 3 tabulates the models and specifications of the components and equipment used in the prototype of the deep learning-driven multiantenna scheme for breast tumor localization, as shown in Fig. 10 (a). Fig. 10 (b) illustrates the in vitro experimental setup with breast replica, where the beige color, white color, green color, and blue dot represent the skin layer, fat layer, gland layer, and tumor, respectively.

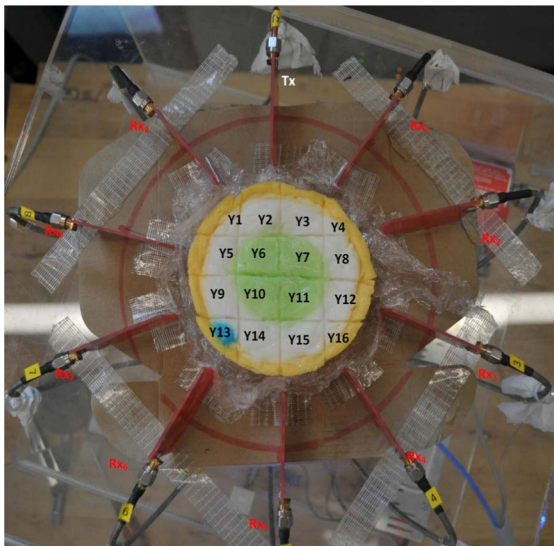
In the in vitro experiment, IR-UWB signals, with an amplitude and pulse width of 1.5 Vp-p and 0.35 ps, are first generated by the pulse generator. The IR-UWB signal is then isolated by the directional coupler into two signals. The first isolated signal is attenuated by –10 dB and fed into the four-channel digital oscilloscope via channel 1 of the digital oscilloscope, while the other unattenuated isolated signal is the input of the Tx antenna.

The signal from the Tx antenna is transmitted through the breast replica to the nine receiving antennas (Rx₁ – Rx₉). The received signals by Rx₁ – Rx₉ antennas are then sequenced by the RF-Switch and fed into the digital oscilloscope via channel 3. The signal data are subsequently retained in the computer via USB-GPIB for subsequent classification by the deep learning algorithmic scheme to localize breast tumor.

Fig. 11 depicts, as an example, the experimental breast replicas without and with cancerous cells in different tissue



(a)



(b)

FIGURE 10. The proposed non-ionic deep learning-driven IR-UWB multiantenna scheme: (a) prototype of the antenna scheme, (b) in vitro experimental setup with breast replica.

layers of the breast, where the beige color, white color, green color, and blue dot represent the skin layer, fat layer, gland layer, and tumor, respectively.

Fig. 12 shows the experimental CT scan machine (Siemens model SOMATOM confidence (512 × 512 slide), KVP (kilovoltage peak) = 120 kVp, generated power = 36 W, exposure = 70 mR, slice thickness = 3 mm) with breast replicas. The 2D CT images are compared with the tumor localization by the proposed deep learning-driven IR-UWB multiantenna scheme, and the results are discussed in the subsequent section.

VI. COMPARISON BETWEEN CT SCANS AND THE DEEP LEARNING RESULTS

To validate the classification performance of the non-ionic deep learning-driven IR-UWB multiantenna scheme, this

TABLE 3. The specifications of experimental components and equipment.

Component/Equipment	Model/Type	Specification
Pulse generator	Anritsu MP1763C	Pulse/Pattern Generator 0.05 – 12.5GHz
Directional coupler	Narda	0.5-18GHz
Digital oscilloscope (ADC)	Tektronix, TDS7404B	Digital Phosphor Oscilloscope (4GHz, 20GS/s)
Tx, Rx antennas	Side slot Vivaldi antenna	2.8-7GHz, Gain 6dBi
RF Switch	DOW-Key Microwave 5A1-5208	DC-18GHz /10-port Microwave Coaxial Switch/SMA/12 Vdc
General port interface bus (GPIB)	Agilent Technologies, 82357B	USB/GPIB interface USB2.0, transfer rate over 850 KB/s

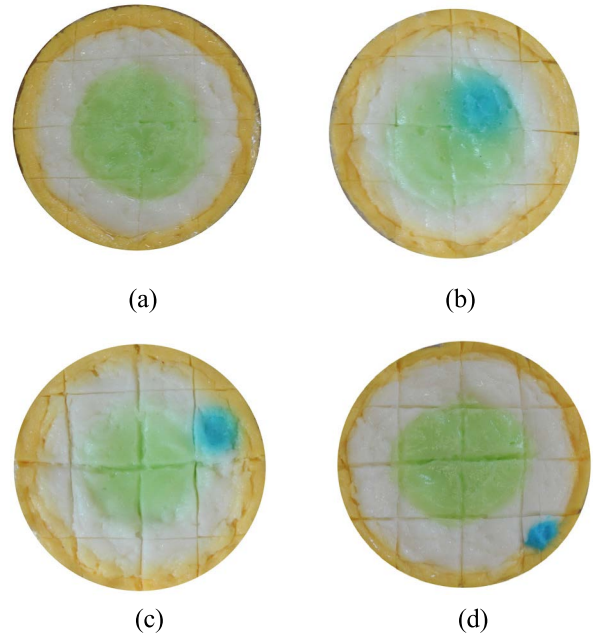


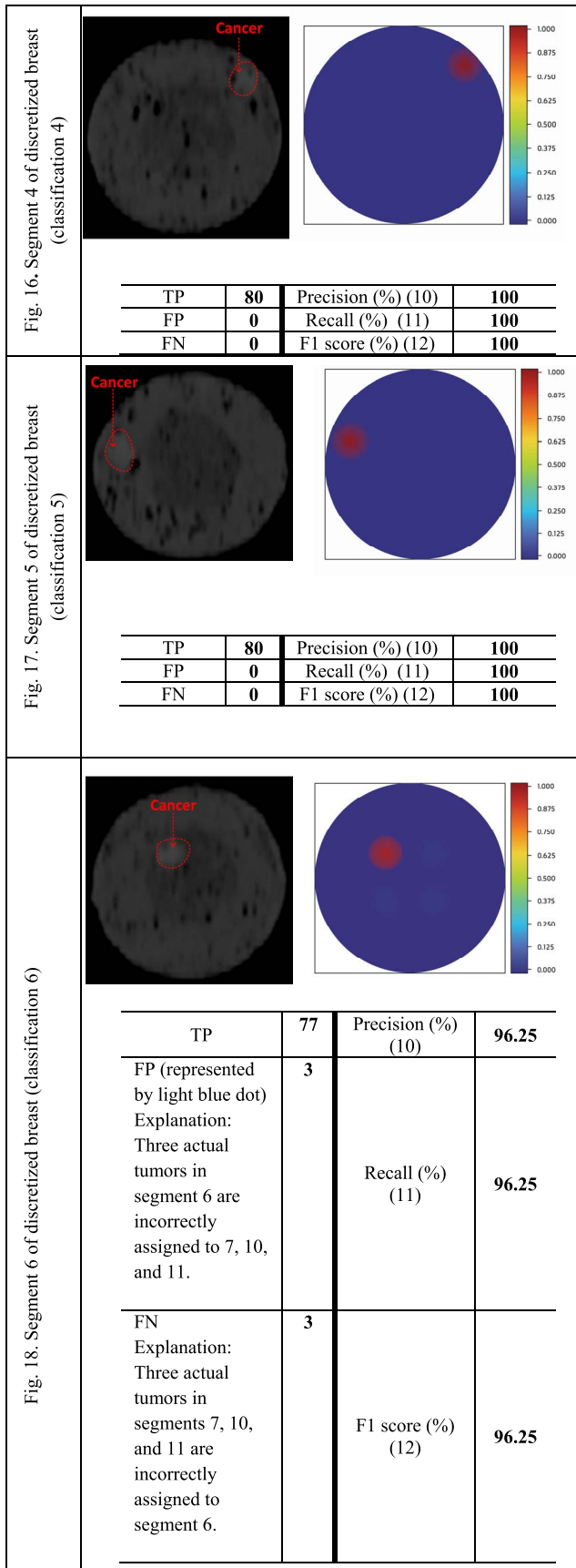
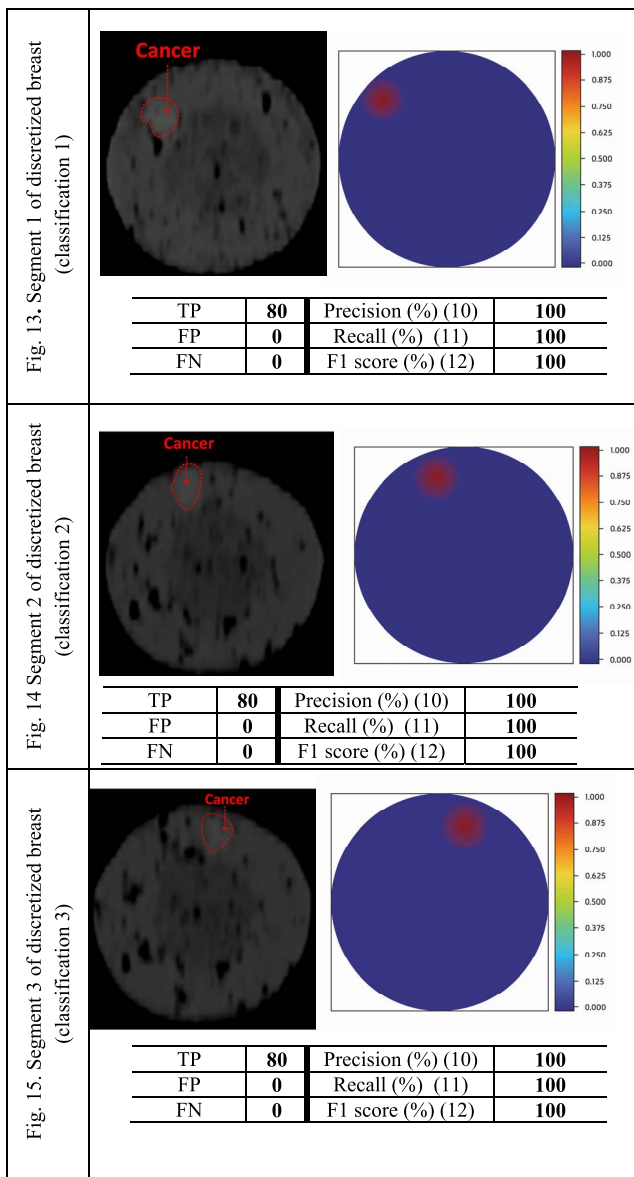
FIGURE 11. Examples of the experimental breast replicas: (a) cancer-free, (b) with tumor in the gland layer, (c) with tumor in the fat and gland layers, (d) with tumor in the fat layer.

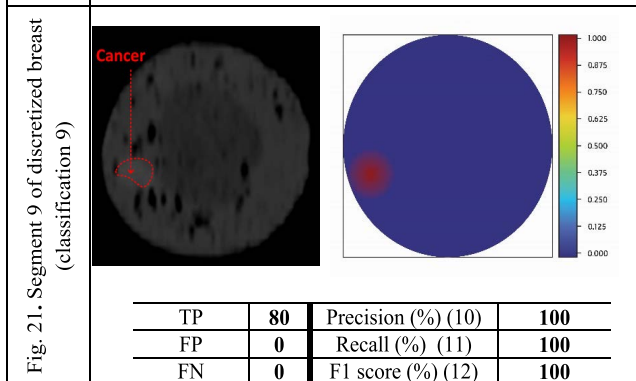
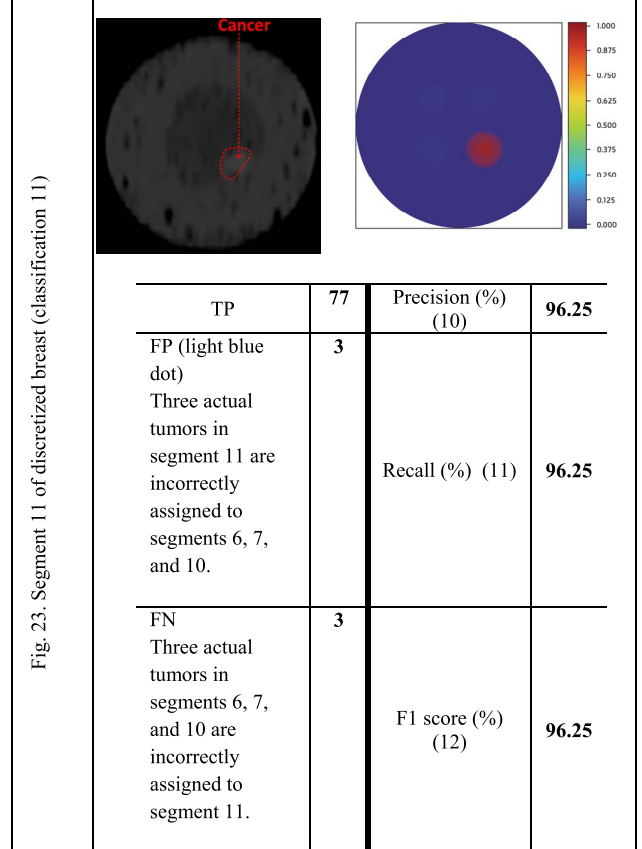
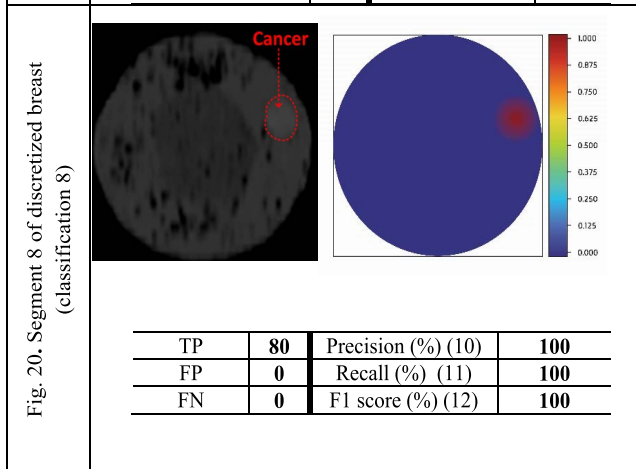
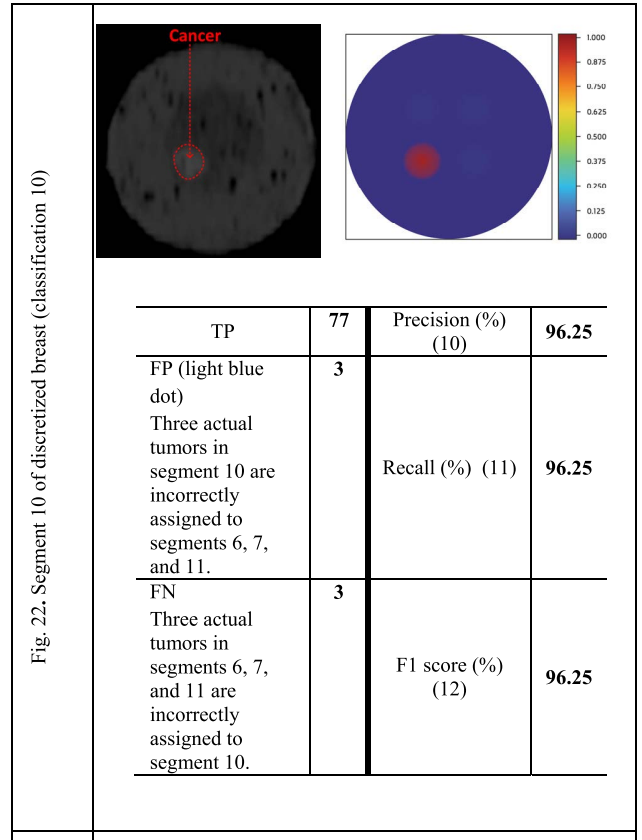
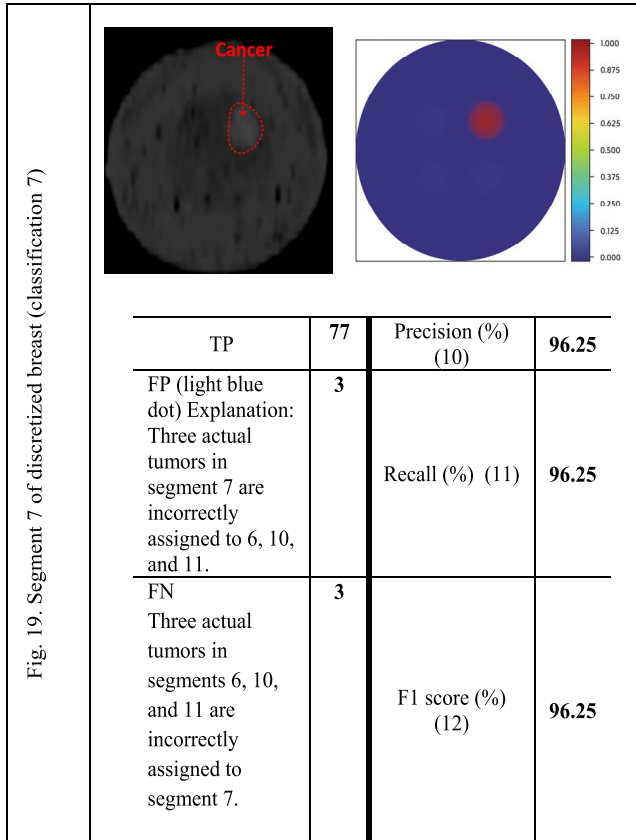
research utilized 8 datasets per classification for evaluation, given 17 classifications (classifications 1 – 17) where classifications 1 – 16 correspond to the 16 discretized segments of the breast and classification 17 represents cancer-free. (Note: TP (true positive) + FP (false positive) = 8 datasets per classification.) Fig. 13 – 29 show the CT scan images and the deep learning-driven classification results of breast replicas for classifications 1 – 17, respectively.

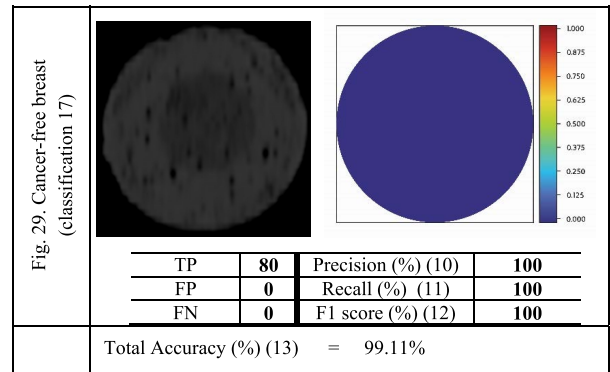
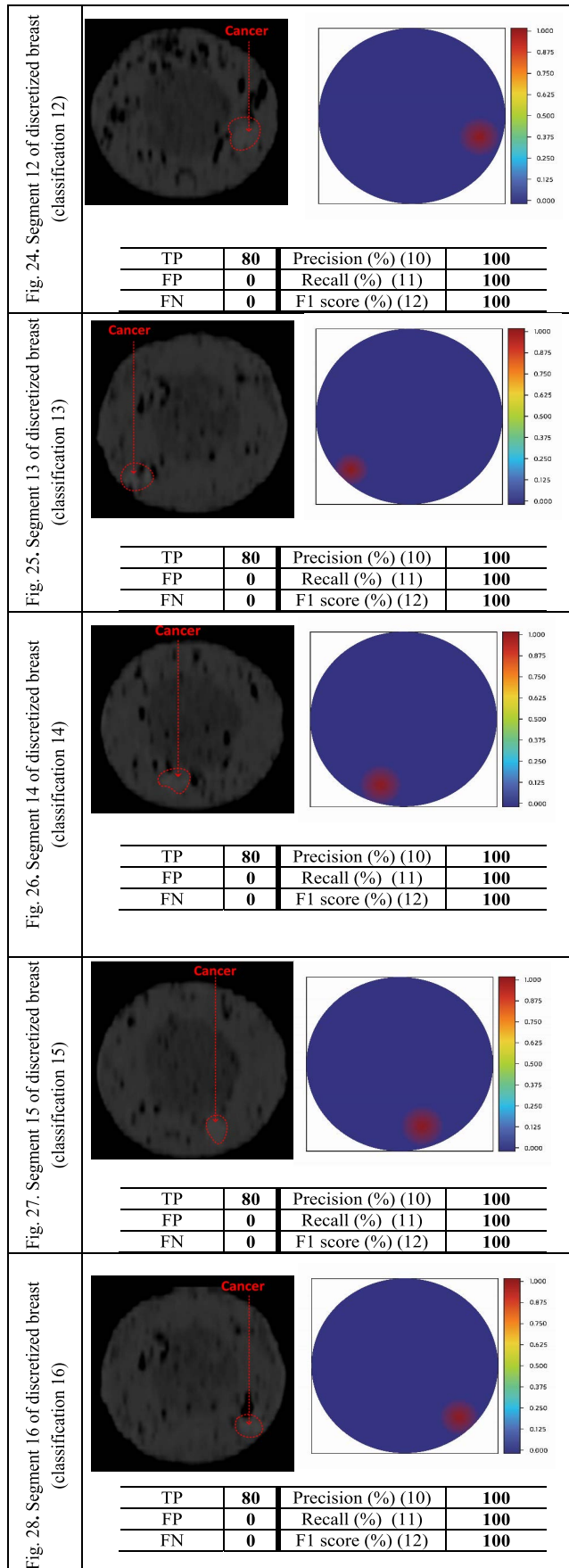


FIGURE 12. The experimental CT scan machine together with breast replicas.

In Fig. 13 – 29, the results show that the proposed deep learning-driven IR-UWB multiantenna scheme could efficiently detect and accurately localize the breast tumor (for







FIGURES 13–29. Comparison between the CT scan images and deep learning classification results of the breast replicas (Note: The detailed definitions of TP, FP, and FN are provided in the Deep Learning Algorithm Evaluation sub-section).

TABLE 4. Comparison between existing studies and current research.

Ref.	Technology	Antenna type	Operating Frequency	Detection Method
[9]	Simulation Time domain UWB signal	1Tx,1Rx Directional antenna	4.0–8.0 GHz	Neural Network
[11]	Time-domain UWB FDTD Simulation	Multi- antenna comparison	Center frequency 3.57 GHz	SVM (Support Vector Machine)
[12]	Time-domain UWB	4 dipole antennas	Center frequency 3.57 GHz	SVM (Support Vector Machine) and LDA (Linear Discrimina nt Analysis)
[14]	UWB image	-	-	Convolutio n Neural Network
[15]	CST Simulation	Bow-tie antenna	3.1–10.6 GHz	K-nearest neighbors
[17]	Time-domain UWB	Aperture array positioned on a section of the hemi- sphere	-	UWB Radar Image
[29]	Time/frequen cy-domain UWB	Slide slotted Vivaldi antenna	2.80-7.00 GHz	Iteratively corrected delay and sum algorithm (IC-DAS)
This study	Non-ionic deep learning- driven time- domain IR- UWB multiantenna scheme	Side slot Vivaldi antennas, consisting of 1 Tx and 9 Rx antennas	2.0-7.0 GHz	Multi-deep learning localization

classifications 1 – 16), as evidenced by the F1 score of 100 %, for almost all classifications except classifications 6, 7, 10, and 11. Besides, in Fig. 29, the proposed multiantenna scheme, given the F1 score of 100 %, also correctly identifies the cancer-free breast replica as non-cancerous (i.e., classification 17). Most importantly, there are no instances in which the deep learning algorithm fails to detect the tumor and erroneously identifies the breast as cancer-free, as evident in FN = 0 (Fig. 29).

However, the performance of the proposed multiantenna scheme is slightly impeded when the tumor resides deep inside the breast (classifications 6, 7, 10, and 11), as evidenced by the F1 scores of 96.25 %, 96.25 %, 96.25 %, and 96.25 %, respectively. Nonetheless, the total accuracy (average of F1 scores) is 99.11%, indicating that the proposed deep learning-driven IR-UWB multiantenna scheme could be deployed to non-ionically diagnose and localize the breast tumor. Meanwhile, the localization of breast tumors by the CT scan machine, as indicated by the contour areas in Fig. 13 - 29, requires the expertise and subjective interpretation of radiologists.

For ease of reference, Table 4 comparatively summarizes the existing studies on non-ionic UWB technologies for breast tumor diagnosis and this current research.

VII. CONCLUSION

This research presents a non-ionic deep learning-driven IR-UWB multiantenna scheme for breast tumor localization. The proposed multiantenna scheme consists of one Tx and nine Rx₁ – Rx₉ antennas. In the diagnosis, the multiantenna scheme is rotated clockwise in 90° increments around the breast, with the Tx angular positions of 0°, 90°, 180°, and 270°, respectively. The deep learning algorithmic scheme yields 17 classification outputs (i.e., 17 classifications), consisting of classifications 1 – 16 which correspond to locations 1 – 16 of the tumor in the breast replicas and classification 17 for cancer-free. The results show that the proposed deep learning-driven multiantenna scheme could efficiently detect and accurately localize the breast tumor (for classifications 1 – 16), as evidenced by the F1 score of 100 %, for almost all classifications except classifications 6, 7, 10, and 11 where the tumors reside deep inside the breast (F1 score of 96.25 % each). Essentially, the total accuracy (average of F1 scores) of the proposed multiantenna scheme is 99.11 %. To address the low F1 scores (for classifications 6, 7, 10, and 11) and improve the total accuracy, subsequent research would experiment with other multi-antenna configurations and re-optimized deep learning algorithms.

ACKNOWLEDGMENT

The author would like to express deep gratitude to Thailand's Siriraj Hospital for expert advice and technical support on CT images.

REFERENCES

- [1] M. Kahar, A. Ray, D. Sarkar, and P. P. Sarkar, "An UWB microstrip monopole antenna for breast tumor detection," *Microw. Opt. Technol. Lett.*, vol. 57, no. 1, pp. 49–54, Jan. 2015.
- [2] H. Zhang, "Microwave imaging for ultra-wideband antenna based cancer detection," *Edinburgh Res. Arch.*, Univ. Edinburgh, U.K., Tech. Rep., 2015.
- [3] C. K. Kuhl, S. Schradang, C. C. Leutner, N. Morakkabati-Spitz, E. Wardelmann, R. Fimmers, W. Kuhn, and H. H. Schild, "Mammography, breast ultrasound, and magnetic resonance imaging for surveillance of women at high familial risk for breast cancer," *J. Clin. Oncol.*, vol. 23, no. 33, pp. 8469–8476, Nov. 2005.
- [4] J. G. Elmore and M. B. Barton, "Ten-year risk of false positive screening mammograms and clinical breast examinations," *New England J. Med.*, vol. 338, no. 16, pp. 1089–1096, 1998.
- [5] D. Arnone, C. Ciesla, and M. Pepper, "Terahertz imaging comes into view," *Phys. World*, vol. 13, p. 35, Apr. 2000.
- [6] G. Geetharamani and T. Aathmanesan, "Metamaterial inspired THz tomography for breast cancer detection," *Social Netw. Appl. Sci.*, vol. 1, no. 6, pp. 1–9, Jun. 2019.
- [7] J. P. Guillet, B. Recur, L. Frederique, B. Bousquet, L. Canioni, I. Manek-Hönninger, P. Desbarats, and P. Mounaix, "Review of terahertz tomography techniques," *J. Infr., Millim., THz Waves*, vol. 35, no. 4, pp. 382–411, 2014.
- [8] A. E. Fouda and F. L. Teixeira, "Ultra-wideband microwave imaging of breast cancer tumors via Bayesian inverse scattering," *J. Appl. Phys.*, vol. 115, no. 6, Feb. 2014, Art. no. 064701.
- [9] S. A. AlShehri and S. Khatun, "UWB imaging for breast cancer detection using neural network," *Prog. Electromagn. Res. C*, vol. 7, pp. 79–93, 2009.
- [10] R. C. Conceicao, M. O'Halloran, M. Glavin, and E. Jones, "Support vector machines for the classification of early-stage breast cancer based on radar target signatures," *Prog. Electromagn. Res. B*, vol. 23, pp. 311–327, 2010.
- [11] D. Byrne, M. O'Halloran, E. Jones, and M. Glavin, "Support vector machine-based ultrawideband breast cancer detection system," *J. Electromagn. Waves Appl.*, vol. 25, no. 13, pp. 1807–1816, Jan. 2011.
- [12] D. Byrne, M. O'Halloran, M. Glavin, and E. Jones, "Breast cancer detection based on differential ultrawideband microwave radar," *Prog. Electromagn. Res. M*, vol. 20, pp. 231–242, 2011.
- [13] J. C. Y. Lai, C. B. Soh, E. Gunawan, and K. S. Low, "UWB microwave imaging for breast cancer detection—Experiments with heterogeneous breast phantoms," *Prog. Electromagn. Res.*, vol. 16, pp. 19–29, 2011.
- [14] E. Govinda and V. S. I. Dutt, "Breast cancer detection using UWB imaging and convolutional neural network," *Ilkogretim Online*, vol. 20, no. 5, pp. 1657–1670, 2021.
- [15] E. A. Aydın and M. K. Keleş, "Breast cancer detection using K-nearest neighbors data mining method obtained from the bow-tie antenna dataset," *Int. J. RF Microw. Comput.-Aided Eng.*, vol. 27, no. 6, Aug. 2017, Art. no. e21098.
- [16] M. R. Al-Hadidi, A. Alarabeyyat, and M. Alhanahnah, "Breast cancer detection using K-nearest neighbor machine learning algorithm," in *Proc. 9th Int. Conf. Develop. eSystems Eng. (DeSE)*, Aug. 2016, pp. 35–39.
- [17] M. Klemm, I. Craddock, J. Leendertz, A. Preece, and R. Benjamin, "Experimental and clinical results of breast cancer detection using UWB microwave radar," in *Proc. IEEE Antennas Propag. Soc. Int. Symp.*, Jul. 2008, pp. 1–4.
- [18] H. Bahramiabarghouei, E. Porter, A. Santorelli, B. Gosselin, M. Popović, and L. A. Rusch, "Flexible 16 antenna array for microwave breast cancer detection," *IEEE Trans. Biomed. Eng.*, vol. 62, no. 10, pp. 2516–2525, Oct. 2015.
- [19] R. C. Conceição, M. O'Halloran, M. Glavin, and E. Jones, "Evaluation of features and classifiers for classification of early-stage breast cancer," *J. Electromagn. Waves Appl.*, vol. 25, no. 1, pp. 1–14, Jan. 2011.
- [20] N. N. Kumar, B. S. Srikanth, S. B. Gurung, S. Manu, G. N. S. Gowthami, T. Ali, and S. Pathan, "A slotted UWB monopole antenna with truncated ground plane for breast cancer detection," *Alexandria Eng. J.*, vol. 59, no. 5, pp. 3767–3780, Oct. 2020.
- [21] S. Brovoll, T. Berger, Y. Paichard, O. Aardal, T. S. Lande, and S.-E. Hamran, "Time-lapse imaging of human heart motion with switched array UWB radar," *IEEE Trans. Biomed. Circuits Syst.*, vol. 8, no. 5, pp. 704–715, Oct. 2014.
- [22] P. Saha, N. Sasaki, and T. Kikkawa, "A single-chip Gaussian monocycle pulse transmitter using 0.18 μm CMOS technology for intra/interchip UWB communication," in *Symp. VLSI Circuits, Dig. Tech. Papers.*, Jun. 2006, pp. 204–205.

- [23] E. C. Fear, X. Li, S. C. Hagness, and M. A. Stuchly, "Confocal microwave imaging for breast cancer detection: Localization of tumors in three dimensions," *IEEE Trans. Biomed. Eng.*, vol. 49, no. 8, pp. 812–822, Aug. 2002.
- [24] Y. Xie, B. Guo, L. Xu, J. Li, and P. Stoica, "Multistatic adaptive microwave imaging for early breast cancer detection," *IEEE Trans. Biomed. Eng.*, vol. 53, no. 8, pp. 1647–1657, Aug. 2006.
- [25] N. Hayashi, Y. Ogawa, K. Kubota, K. Okino, R. Akima, S. Morita-Tokuhiro, A. Tsuzuki, S. Yaogawa, A. Nishioka, and M. Miyamura, "Computed tomography demonstration of the production and distribution of oxygen gas following intratumoral injection of a new radiosensitizer (KORTUC) for patients with breast cancer—Is intratumoral injection not an ideal approach to solve the major problem of tumor hypoxia in radiotherapy?" *Cancers*, vol. 8, no. 4, p. 43, Apr. 2016.
- [26] T. Guswantoro, A. S. Supratman, and I. S. Asih, "Measurement the Hounsfield unit of alginate impression material using CT-scan equipment to find equility with the human body tissue," in *Proc. Adv. Social Sci., Educ. Humanities Res.*, Jun. 2021, pp. 361–364.
- [27] M. J. Yaffe, "Contrast-enhanced dedicated breast CT: Initial clinical experience," *Breast Diseases, Year Book Quart.*, vol. 22, no. 4, pp. 374–375, Jan. 2011.
- [28] M. T. Islam, M. Samsuzzaman, S. Kibria, and M. T. Islam, "Experimental breast phantoms for estimation of breast tumor using microwave imaging systems," *IEEE Access*, vol. 6, pp. 78587–78597, 2018.
- [29] M. T. Islam, M. Z. Mahmud, M. T. Islam, S. Kibria, and M. Samsuzzaman, "A low cost and portable microwave imaging system for breast tumor detection using UWB directional antenna array," *Sci. Rep.*, vol. 9, no. 1, pp. 1–13, Dec. 2019.
- [30] R. Vijay, R. Jain, and K. Sharma, "Dielectric properties of water at microwave frequencies," *Int. J. Eng. Res. Technol.*, vol. 3, no. 3, pp. 312–317, 2014.
- [31] A. Rittiylang and P. Phasukkit, "Solving for complex permittivity of biomedical tissue from open-ended probe measurement," in *Proc. Int. Symp. Multimedia Commun. Technol.*, Aug. 2017, pp. 1–4.
- [32] R. Zajicek, L. Oppl, and J. Vrba, "Broad-band measurement of complex permittivity using reflection method and coaxial probes," *Radioengineering*, vol. 17, no. 1, pp. 14–19, Apr. 2008.
- [33] M. Kamphong and P. Phasukkit, "Development of phantom model for the dielectric property measurement," in *Proc. Int. Symp. Multimedia Commun. Technol.*, Aug. 2017, pp. 75–78.



PATTARAPONG PHASUKKIT (Member, IEEE) was born in Saraburi, Thailand, in May 1978. He received the B.Eng. and M.Eng. degrees in telecommunications and the D.Eng. degree in electrical engineering from the Department of Electronics, School of Engineering, King Mongkut's Institute of Technology Ladkrabang (KMITL), Bangkok, Thailand, in 2000, 2003, and 2009, respectively. He is currently working as an Associate Professor with the Department of Electronics, School of Engineering, KMITL. His current research interests include microwave ablation, antenna design, and UWB radar application.

• • •